IEEE Access
Multidisciplinary ⋮ Rapid Review ⋮ Open Access Journal

Received 13 March 2026, accepted 10 April 2026. Date of publication 00 xxxx 0000, date of current version 00 xxxx 0000.

Digital Object Identifier 10.1109/ACCESS.2026.3689679

Satellite-Based Processing Pipeline for Assessing Water Turbidity in Rivers

G. TRIBOLI[1], M. PICONE[2], AND M. BERTOGNA[1]
[1]Department of Physics, Informatics and Mathematics (FIM), University of Modena and Reggio Emilia, 41125 Modena, Italy
[2]Department of Sciences and Methods for Engineering (DISMI), University of Modena and Reggio Emilia, 42122 Reggio Emilia, Italy
Corresponding author: G. Triboli (giovanni.triboli@unimore.it)

ABSTRACT Modern agro-industrial and livestock practices based on intensive production models cause uncontrolled downstream diffusion of substances through water systems—compounds that are often overused to enhance productivity. Although these substances have a high fertilizing effect, they also produce excessive and undesirable environmental impacts. Among these, eutrophication is a growing concern for aquatic ecosystems, as it frequently triggers rapid and extensive growth of aquatic vegetation and intensifies sedimentation processes, leading to difficulties in navigation and water flow. Detecting and quantifying such phenomena is essential for effective water quality monitoring. Solid nutrient compounds can be transported over long distances through canals and rivers, affecting water turbidity. This study presents an automated tool that employs satellite imagery to observe and quantify turbidity levels and their spatiotemporal variations in river systems through the application of an original processing pipeline. The vastness of the datasets available on satellite processing platforms and the complexity of the computational primitives available for their processing require a structured approach to implement an effective research project. The literature refers to this method as a processing pipeline, a well-defined workflow that includes four distinct phases that enable the identification of suitable sources, screening of relevant data, extraction of the required information, and delivery of this information in the most usable form to uncover insights into the topic under study. The proposed approach integrates classical indices from the scientific literature with data from the widely used OpenStreetMap dataset. The methodology involves selecting high-resolution satellite images within a defined spatiotemporal window, ensuring data quality by filtering out cloud-covered imagery through the use of a dedicated spectral band. The tool was applied to a case study covering the upper 44 kilometers of the Mincio River, from Lake Garda to the outskirts of Mantua, during 2023–2024 in the Po Valley, Italy. The method introduces an innovative technique that, by leveraging the georeferenced vector dataset, enables precise calculation of the Normalized Difference Turbidity Index (NDTI) along the river course. An additional novel segmentation phase divides the river surface into a linear sequence of fixed-length sections, on which mean NDTI values are computed. This allows for a detailed assessment of how turbidity changes when the river encounters effluents, urban centers, drainage canals, and dams, and varies across different seasons. The processing pipeline also includes post-processing steps designed to refine, integrate, and graphically present the results for effective interpretation of the turbidity peaks detected every 500 meters of the river, which are unraveled across space and time, and show the intensity and speed of the phenomenon, even in 3D. Although current findings are preliminary, the study highlights potential future improvements, including a simplified user interface and broader applications aimed at making the tool more accessible and versatile for large-scale environmental monitoring activities.

INDEX TERMS Automated environmental monitoring, eutrophication, google Earth engine, NDTI, river turbidity, satellite remote sensing.

I. INTRODUCTION

In recent decades, lakes and rivers have increasingly suffered eutrophication from excessive anthropogenic nitrates and

The associate editor coordinating the review of this manuscript and approving it for publication was Stefania Bonafoni.

phosphates. This enrichment, mainly driven by persistent agricultural mismanagement and fertilizer overuse, harms aquatic ecosystems, navigation, and hydrogeological stability. Industrialized Western countries, especially those with livestock concentrated in Concentrated Animal Feeding Operations (CAFOs), generate large amounts of polluting waste [1]. The Po Valley in Lombardy is a critical hotspot: although it covers only 5% of Italy, it hosts 48% of the country's eight million pigs. This livestock farming produces manure rich in nitrate fertilizers and harmful bacteria [2], which is commonly applied to fields via fertigation. When fertigation is synchronized with crop nutrient demand—typically in summer—it can benefit yields, but poor timing or excessive application causes severe environmental pollution [3].

A key problem is the seasonal mismatch between manure production and the soil's capacity to absorb it. EU regulations ban the winter spreading of livestock effluents [4] because impermeable soils favor pollutant volatilization and atmospheric particulate formation. Manure must therefore be stored until February, when large-scale spreading resumes. Nitrogen in liquid manure is more volatile than in synthetic fertilizers [5]; part contributes to particulate matter [6], while another part leaches into groundwater [7]. The most visible impacts occur in rivers and lakes [8], [9], where nutrients drive excessive aquatic vegetation, sedimentation, and navigation problems—especially in dry seasons (Fig. 12), as reported by local media.[1] These processes also heighten flood risk. The eutrophic lakes around Mantua (Italy) show abnormal macrophyte growth (Fig. 1) due to shallow, slow-moving waters, similar to conditions in [10] and [11]. This vegetation reduces light penetration and oxygen, threatening aquatic life [12].

Redistributing livestock could reduce nitrate input but remains economically unfeasible. Instead, mitigation strategies include solidifying manure with zeolite-based technologies to enhance soil nitrate retention [13], applying Precision Livestock Farming [14], and using planning tools to better align manure application with crop uptake, considering soil, weather, storage, and fleet logistics [15]. IoT integration can further optimize and certify application processes [16], [17].

This paper addresses these environmental challenges by examining the turbidity of the Mincio River, which feeds the Mantuan lakes and flows through a heavily industrial and agricultural region. Although turbidity is a key indicator of water quality and suspended solids, river transparency r emains relatively underexplored due to the effort required to assess a long river over an extended period. This circumstance stimulated this study to produce an automated tool for assessing river turbidity using relevant satellite imagery over the target Region of Interest (ROI), as shown in Fig. 2, to analyze seasonal dynamics throughout the year 2024. As anticipated in the summary, the workflow

[1]YouTube Gazzetta di Mantova (2022): https://www.youtube.com/watch?v=pzihTLucPVA

(a) Mantua and its lakes. An area affected by abundant vegetation growth is outlined in red.

(b) The green carpet. Satellite view

(c) The green carpet. Drone view

FIGURE 1. Summer macrophyte islands invade the lake surface, causing bottlenecks, and anoxia.

follows a standard four-step procedure, conventionally called a pipeline, whose original implementation is represented in Figure 3. The main operations conform to this scheme to efficiently collect, filter, process, and output data, which are outlined from here on. The system filters cloud-covered images through a dedicated spectral band for cloud detection, ensuring high-quality data. The proposed method combines established remote sensing (RS) indices, such as the NDTI, but introduces an original approach to focus on river surfaces, effectively segmenting the river course and reporting mean turbidity values for river reaches of predefined and freely configurable lengths.

The NDTI index is extracted and returned in tabular format, accompanied by geographical characteristics to precisely identify the analyzed reaches of the river to which the data refer. As a result, areas of the river with the greatest turbidity

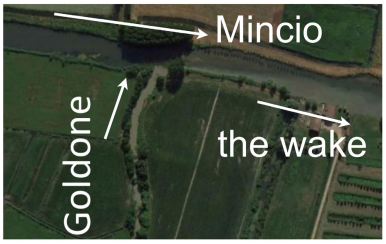

(a) A drone captured the dense waters of the Goldone canal flowing into the Mincio

(b) The Mincio river and tributaries in an OpenStreetMap tile. The arrows indicate the direction of water flow

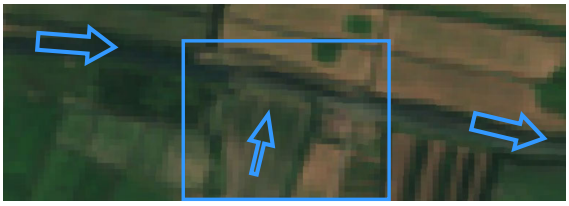

(c) The True Color Copernicus image with a Ground Sample Distance (GSD) of 10 meters

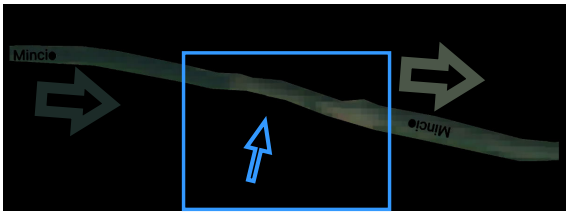

(d) The river color turns lighter because of the high-turbidity tributary. Only by masking the background, it becomes evident

FIGURE 2. The research challenge: a tool to follow the river, within satellite imagery, and transform the pixels into meaningful turbidity data. High levels of turbidity are manifested by clearer waters. The wake is visible in the receiving river.

variations were identified and linked to inflows from adjacent tributaries, canals, and populated areas.

The post-processing phase further refines and integrates the extracted data, improving the overall quality of the outcomes illustrated in the dedicated section V-E, also represented through a series of ad hoc visual elements that facilitate the interpretation of the results. Maps and graphs show the locations of points along the river where the most intense turbidity fluctuations occur, depicting the temporal and spatial evolution of these peaks. Although the current results are preliminary, future developments will include a simplified user interface and extended applications, making the tool increasingly suitable for large-scale environmental monitoring activities.

II. CONTEXT AND MOTIVATION

A. THEORETICAL ASPECTS

This study focuses on the turbidity of surface water bodies, employing a specialized remote sensing tool designed to operate in fluvial environments that are clearly visible in satellite imagery. Vegetation covers approximately one-third of the Earth's surface, while water bodies account for about 71%, encompassing oceans, rivers, lakes, and wetlands [18]. Territories—especially under the current pressures of climate change—depend on these natural resources for their sustainability and prosperity. Water bodies provide freshwater and support ecosystems [19]; together with vegetation, they are fundamental to human life, wildlife, and planetary health. They play a crucial role in climate regulation, agricultural productivity, and the maintenance of natural habitats. Due to their ubiquity and ecological significance, both water and vegetation have long been central subjects of scientific investigation.

Over the past several decades, a constellation of Earth-observing satellites has provided researchers with precious datasets. Among the best-known and most widely used missions are the European Space Agency's (ESA) Copernicus satellite, the American Landsat satellite of the United States Geological Survey (USGS), and the MODerate-resolution Imaging Spectroradiometer (MODIS) of the National Aeronautics and Space Administration (NASA). Planetary-scale imagery can be processed to derive numerous remote sensing indices [20] for environmental monitoring. In this study, the Normalized Difference Turbidity Index (NDTI) was used to estimate river turbidity and its spatiotemporal variability, following the formulas in the "Evaluation Metrics" section. Because transparency indirectly reflects overall water quality, large decreases in transparency can indicate pollution events.

In parallel, the Normalized Difference Water Index (NDWI) was computed to detect and monitor water extent and depth, and the Normalized Difference Vegetation Index (NDVI) to quantify vegetation presence, health, and density, including some aquatic vegetation.

According to Scopus, these indices are widely used in remote sensing. By the end of 2025, NDVI appears in about 40,000 publications, NDWI in over 3,000, and both together in about 1,700. Turbidity is less studied: NDTI appears in roughly 300 publications—about 60 with NDVI, 30 with NDWI, and only 13 discussing all three indices together.[2] These are primarily environmental studies. They range from monitoring lake vegetation in relation to fertilizer consumption and climate change to mapping urban quality of life. They also focus on the decline of urban vegetation, changes in precipitation patterns, and the concomitant increase in surface temperatures, or use RS

[2]Scopus query https://www.scopus.com/results/results.uri?st1=NDVI+and+NDWI+and+NDTI&st2=&s=TITLE-ABS-KEY%28NDVI+and+NDWI+and+NDTI%29

indices to classify basins based on turbidity levels or water cover according to vegetation type, or to map mangrove areas.

B. OPEN CHALLENGES

The work described in this article constitutes a remote sensing project designed to extract information from satellite imagery through scripts executed on the Google Earth Engine (GEE) platform:[3] The code performs all the tasks described in the processing pipeline stages, illustrated in the specific section. In essence, (1) the script retrieves the images, (2) keeps only the appropriate ones, (3) identifies the pixels representing the river course and (4) calculates the values of the required RS indices, (5) averaging them over 500-meter-long river stretches. Despite GEE remarkable capabilities, several challenges were encountered and addressed during development.

A key issue was intermittent data loss during frequent exchanges with GEE servers. To address this, a continuous saving mechanism was implemented, preserving data integrity and allowing processing tasks to be paused and resumed without losing results. This was crucial because GEE's limitations regarding local data exports make it incompatible with the full length of the river and the required spatial resolution. As a result, batch processing followed by a merging phase was necessary. Another major challenge involved image masking requests, among the most computationally demanding GEE operations. Because the project computes turbidity with high precision for individual river segments, clipping operations must be performed frequently. To reduce processing overhead, the length of the river sections was chosen to be 500 meters. This is a reasonable compromise: not too long to lose the ability to identify turbidity peaks, but not too short to produce too many observation lenses, making processing unacceptably slow. To achieve an efficient solution, a more advanced approach would download the full turbidity index image for the river in segments and perform local segmentation offline, replicating GEE's functionality with equivalent Python libraries and APIs.

A key difficulty was developing the river segmentation algorithm. As described in the pipeline, the method uses a sequence of circular lenses, but tangency between adjacent lenses is sometimes lost, causing large overlaps. Removing this inaccuracy requires a more refined segmentation algorithm.

Another challenge emerged from the turbidity index (NDTI) analysis. The algorithm computes mean NDTI values along 88 segments covering the 44 km study reach. Many turbidity increases noted in Section Analysis of Turbidity Spikes occur near tributary confluences, with similar peaks at major hydraulic drops; in many cases, turbidity returns to baseline within about one kilometer. It would be useful to quantify how much of these increases are due to natural mixing to better estimate the pollutant load from tributaries. The greatest challenge is to determine the share attributable to human activities.

[3]Google Earth Engine https://earthengine.google.com/

C. EXISTING APPROACHES & RESEARCH OPPORTUNITIES

This project obtains accurate, georeferenced measurements of river turbidity by integrating two public datasets. Satellite rasters processed with remote sensing indices are restricted to areas of interest defined by a cartographic database. A review of river and lake remote sensing shows diverse approaches, but the proposed method is still original.

Beyond reviews, several works assess specific RS indices under varying conditions—e.g., NDWI and NDVI in [21], and NDVI-derived indices (GNDVI, WAVI) for salt marsh detection in [22]. Other studies use these indices to validate or complement different methods or to propose new formulations through comparative or hybrid approaches. Relevant examples are in Section III.

Each approach advances the field, though accuracy and applicability differ by index. The Normalized Difference Turbidity Index (NDTI) has key limitations, addressed here as follows:

- *Atmospheric interference and surface variability:* Atmospheric conditions and surface radiometry (water vapor, emissivity) introduce uncertainty. This study reduces these effects by selecting images via the Copernicus dataset's quality assessment band (Section PREPROCESSING PHASE)).
- *Classification ambiguities:* NDTI can misclassify vegetation, shadows, or artificial surfaces as water, especially in heterogeneous areas, leading to an overestimation of water extent. This was mitigated by delineating river boundaries using the cartographic database and the algorithm in Section Feature Extraction Phase.
- *Qualitative nature:* NDTI generally yields qualitative, not quantitative, turbidity estimates, which is acceptable for this study's scale and goals.
- *Validation:* Differences between NDTI values and actual turbidity require complementary in-situ measurements and collaboration with local experts to validate automated results.

These issues highlight the need for improved index calibration and validation in future work.

D. SPECIFIC OBJECTIVES

This study analyzes turbidity and its dynamics in surface waters using remote sensing through a dedicated tool that can be further refined for better performance. Its main (partly ongoing) objectives are:

- *Tool flexibility in remote sensing indices and areas of application:* The current algorithms estimate turbidity only at the river surface but can be extended with additional indices compatible with the satellite spectral bands. The tool also enables easy selection of river segments via configurable parameters.

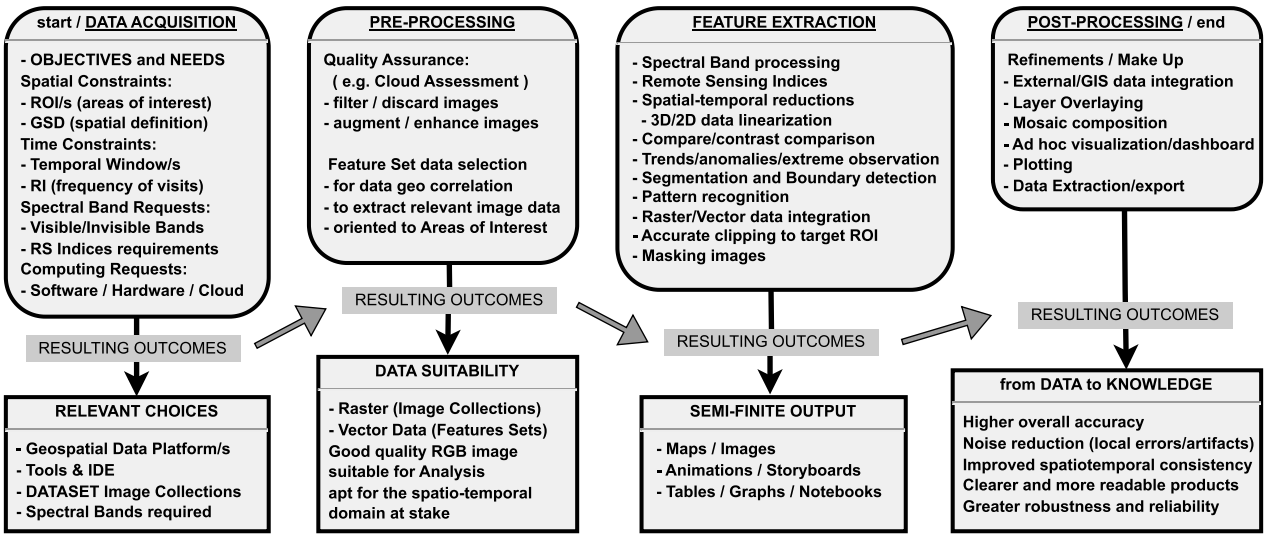

FIGURE 3. The workflow of a Remote Sensing project: the processing steps, needs, output, and common outcomes.

- *Rich result outputs:* The system generates raw tables, maps, composite and hybrid mosaics, and graphical visualizations, improving interpretability and analytical potential.
- *Accessibility for the research community:* Substantial engineering is needed to move beyond the prototype stage. The tool will later be released to researchers for evaluation and use, with a user-friendly interface that abstracts GEE platform complexity.

III. RELATED WORKS

Recent advances in remote sensing now allow precise assessments of water quality and turbidity in rivers and lakes. Many studies, including this one, use indices such as the Normalized Difference Turbidity Index (NDTI) in different analytical frameworks. Reference [23] analyzed turbidity in Indian tropical reservoirs (2016–2021) with the Google Earth Engine (GEE) and Copernicus data, combining the Modified Normalized Difference Water Index (MNDWI) with in-situ validation from the EOMAP water quality portal. They classified reservoirs by turbidity and provided a benchmark for testing optical indices under varying conditions. Reference [24] studied an Indonesian river subject to strong anthropogenic pressures from mining, port, and industrial activities. Using GEE and Sentinel imagery, they applied GIS-based visualization to delineate a river course that is otherwise indistinct in post-processed NDTI imagery. Their turbidity values (253.57–437.80 NDTI units), although not on standardized scales, closely matched the relative variations observed here, confirming the consistency of remotely sensed turbidity patterns across different settings. Reference [25] used remote sensing to measure turbidity and chlorophyll—key indicators of water quality and land-cover change—in a Bolivian Andean lake. Reference [26] used Sentinel imagery (2021) and vegetation- and water-related indices (NDVI, GNDVI, NDAVI, GRVI, NDWI) to detect duckweed infestations in Portugal's Lis River. Given its morphological similarity to the Mincio and the Po Valley, this work underscores the value of remote sensing when field surveys are limited by accessibility. For large-scale applications, remote sensing offers broad spatial coverage, frequent revisits, and lower costs than conventional methods. Building on this, the present study adopts the classical NDTI but refines it by spatially constraining the analysis to the riverbed (Fig. 8). This improves NDTI interpretability, turbidity mapping, and the detection of seasonal changes, localized disturbances, and their propagation along the river. This enhanced detection capacity deepens understanding of turbidity's spatiotemporal dynamics and anthropogenic drivers. The proposed method supports the quantification of agricultural and industrial impacts, to be further validated with in-situ measurements, and is designed to scale to lacustrine environments.

IV. PROCESSING PIPELINE

Over several decades, satellite missions have produced extensive georeferenced imagery covering nearly the entire Earth. These data are distributed through dedicated platforms, enabling a growing body of research across many disciplines. Such platforms typically offer raw and pre-processed datasets and the computational resources to manage them via comprehensive programming interfaces, with some platforms freely accessible to accredited researchers.

This wealth of data and processing options is valuable but can overwhelm newcomers, demanding careful analysis, time, and a structured learning approach. A typical remote sensing workflow has four main stages, discussed in this section and shown in Fig. 3: **Data Acquisition, Pre-processing, Feature Extraction, and Post-processing**. These stages cover the retrieval of relevant imagery, its

refinement, the extraction of target information, and the preparation and dissemination of results.

The specific workflow implementation varies significantly with the application domain and the type of information to be extracted.

A. DATA ACQUISITION PHASE

This chapter describes data access, illustrated in Fig. 4, which highlights three key aspects of effective integrated analysis. The images to be processed are stored in satellite datasets, each containing large collections of images acquired over decades. Thanks to their orbital coverage, these datasets often span most or all of the Earth's surface, as schematically shown in the figure. Efficiently exploring these data to find only the most relevant images (sometimes just a few hundred or even a few dozen) is essential, as it focuses processing on the strictly necessary subset, optimizing platform resources while reducing both processing time and costs.

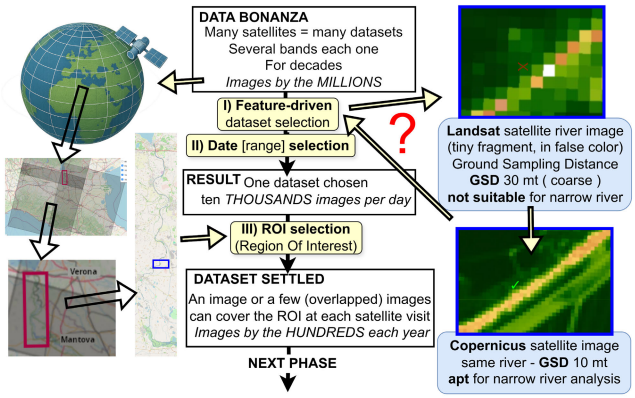

FIGURE 4. Schematic illustration of the Data Acquisition Phase: three main aspects the chosen dataset must address to meet the project requirements.

Because these datasets are highly diverse, selecting those suitable for a specific study requires an initial analysis of metadata describing their spatial, temporal, and spectral characteristics. This metadata is typically accessed through queries via APIs provided by the remote sensing platforms.

The temporal availability of a dataset depends on the satellite's operational period and orbital path, which determine the frequency of revisits to a given location—known as the Revisit Interval (RI). This interval is also affected by the extent and position of overlap areas. Usually on the order of a few days, the RI varies with the region studied and is further influenced by the combined operation of satellite constellations, making it complex to determine. A suitable dataset must match the required temporal span, which may range from decades for long-term trend analyzes to just a few days for one-off events.

These datasets are multispectral because they include several measurement bands, each corresponding to a different electromagnetic frequency detected by onboard sensors. For example, the widely used MultiSpectral Harmonized Sentinel-2 dataset provides 26 bands, individually accessible and combinable—typically to compute composite indices—as they are already harmonized at specific spatial resolutions.

Each pixel—the basic element of a raster grid—represents a square area of the Earth's surface, with a Ground Sampling Distance (GSD) between 10 and 500 meters, which strongly affects possible applications. Sometimes it is enough to verify that the images cover the entire area of interest, such as an

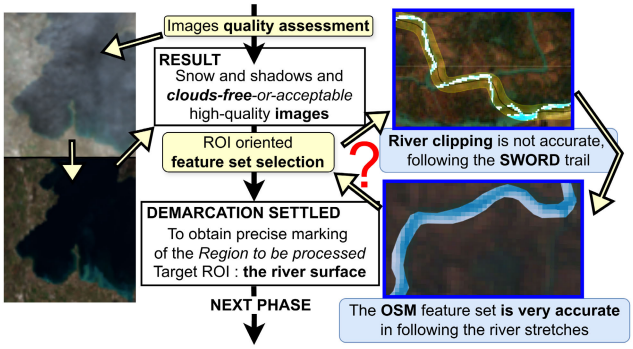

FIGURE 5. A representation of the Preprocessing Phase: two elements that are particularly critical for the study described here are highlighted.

administrative region. Other analyses are more demanding, for instance tracking a complex polygon describing a river course, as in this work. In such cases, it is crucial to ensure that the spatial resolution, determined by sensor sensitivity, is sufficient to support the desired conclusions. The figure refers to the two satellites considered in this study. Only one dataset was suitable: the Copernicus mission, whose resolution is high enough to follow even a narrow river like the one examined here.

The data acquisition phase selects potentially suitable datasets and identifies the useful image subsets. Once an image is chosen, it is usually cropped to the Region of Interest (ROI), outlined in red in the illustrative figure (bottom left), which includes the river segment under study. The actual ROI analyzed here is shown in Fig. 13 and Fig. 14c.

B. PREPROCESSING PHASE

The pre-processing phase ensures the quality of the dataset for the study's spatio-temporal window. It verifies that satellite images meet quality criteria, discarding, correcting, or supplementing them as needed. Cloud cover, provided in the metadata, is a frequent issue affecting multiple spectral bands in both visible and non-visible ranges and is almost unavoidable. With large image sets, only cloud-free scenes may be retained; if too few remain, images from other datasets with compatible bands can be added. Partially cloudy images can be processed with filters to reconstruct affected areas.

Some datasets only report an average cloud value for the entire image, making retention decisions difficult. A more effective option occurs when a dataset provides a dedicated cloud mask band (internally or via auxiliary data), with

per-pixel or cluster-based cloud intensity. In the "QA60" band of the dataset mentioned earlier, cloud cover is given at a 60 m resolution, so each value averages a 6×6 pixel block of a 10 m spectral band. These dedicated cloud bands allow for precise cloud coverage estimates over specific regions of interest (ROI), improving data selection. This is crucial because satellite scenes typically cover very large areas (e.g., Copernicus missions image about 110 km × 110 km; see Fig. 6a), while use cases like this study—short river reaches or small lakes—have ROIs about two orders of magnitude smaller. With such a disparity, local cloud intensity must be evaluated to choose images for the time window, as it can differ greatly from the scene-wide average, as shown in Fig. 6.

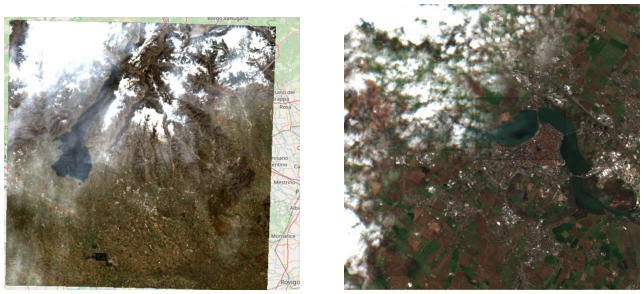

(a) A full image with a tiny ROI (b) The small Mantuan ROI

FIGURE 6. Clouds considerations. a) The full image Copernicus shot on 13-02-2019. Overall cloud intensity at 70%. Despite this, the ROI is clear, the small, barely perceptible black area. b) On the contrary, on 04-03-2020, a slightly cloudy day (20% overall), the lake in the ROI area is quite noisy.

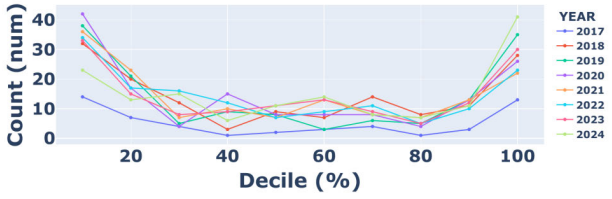

(a) Annual distribution of cloudy days for the small Mantua ROI. Clear days (left side of the graph) are the majority.

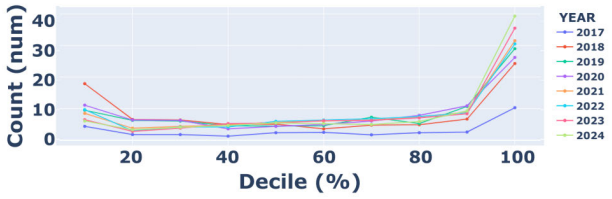

(b) Cloudy days distribution in London.

FIGURE 7. Cloud cover comparison. Most images of Mantua are processable, whereas London is affected by much more challenging weather conditions.

Cloud distribution within a single image can vary greatly, not only with image size but also due to territorial factors (e.g., high mountains in only part of the scene) and climatic conditions. Figure 7 compares the cloud footprint of two contrasting areas: the Mantua river section analyzed in this study and the city of London.

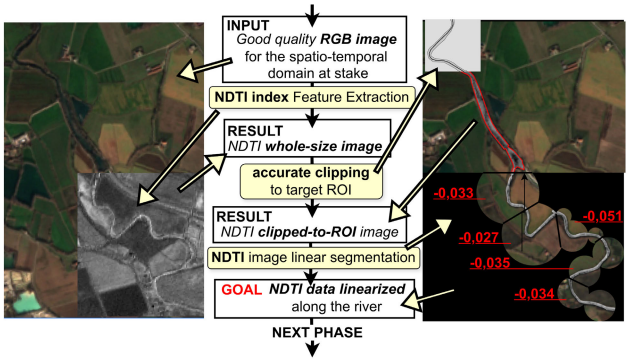

FIGURE 8. Schematic drawing of the Feature Extraction Phase: the steps to transform high-quality raster images into relevant, standardized information. Data from the smaller lenses are normalized before being returned.

This study analyzes water in a small river. To extract the required indices, calculations had to be limited precisely to the river segments visible in the satellite images. For this purpose, dedicated vector datasets were used. Unlike satellite imagery, they do not contain rasters but extensive vector data linked to geographic polygons (e.g., administrative regions, watersheds, ecoregions, and artificial structures). These vector datasets must be combined with raster data and cover topics ranging from ecological footprints to dam locations and socio-economic indicators, providing essential georeferenced features.

The Surface Water and Ocean Topography (SWOT) database—specifically its SWOT River Database (SWORD) derivative—was initially considered but proved insufficiently accurate in following the river's meanders. The study, therefore, relied on the more widely used OpenStreetMap (OSM) database, although it is not directly integrated into the satellite platform adopted, Google Earth Engine (GEE), as illustrated in Fig. 5.

Once the multipolygon has been precisely segmented, preprocessing defines the River Stretch Area of Interest (RSOI).

Pre-processing improves the quality of images selected during data acquisition but can also reduce the dataset to an unacceptably small size, especially under strict cloud-threshold criteria. A temporal summary of the remaining images is therefore necessary to evaluate whether an alternative dataset should be used.

C. FEATURE EXTRACTION PHASE

The feature extraction phase processes the data acquired in the previous steps. The images must be sufficiently numerous and of adequate quality for the research goals and space-time requirements, for example at least one image per month with a pixel resolution of at least 10 meters. The Feature Extraction phase transforms raw data into meaningful information through various operations. Besides using the dataset's native bands, custom indices can be derived by combining bands with specific formulas. Hundreds of such

indices exist in the literature (e.g., [20]), and new ones are continually proposed. In this phase, the most suitable index for the research objective is selected, as each domain requires different approaches. Water-related indices are especially common and widely used. In this study, the Normalized Difference Water Index (NDWI) was computed, but greater emphasis was placed on the Normalized Difference Turbidity Index (NDTI), which is particularly suitable for estimating silt or other suspended particle concentrations in water bodies. As these particles are often linked to anthropogenic activities, the index is highly relevant for water quality monitoring. It exploits the red and near-infrared spectral bands.

Fig. 8 shows the steps of this phase. First, an index image is generated from the RGB pixels of the satellite data; on the left, the figure displays NDTI values in grayscale for part of the image. Then, spatio-temporal reductions—such as mean values—are applied to enable comparisons across areas or time intervals, supporting the detection of trends, anomalies, or extremes in the subsequent post-processing phase. For example, locations along the river with maximum turbidity variation were identified and related to tributary inflows, discharges, or nearby settlements. Achieving this required addressing two main challenges.

The first challenge was isolating river pixels in the image to avoid including unwanted soil contributions in the mean NDTI values. To do this, the river vector profile from the OSM database was used. In Google Earth Engine (GEE), the GPS coordinates were converted into a polygon and applied as a clipping mask to the NDTI image. In the upper-right panel of Fig. 8, the river profile is shown for a short reach in a small gray inset. The river course is traced in red on the full-color satellite image, with the interior overlaid in grayscale to represent NDTI values. This combination of multiple information layers in a single image is called mosaicking. The result is a clipped NDTI image: a grid of gray pixels for the river and black pixels for the background.

The second challenge was converting the clipped NDTI pixels into a linear set of numerical values representing the mean NDTI at the desired scale, i.e., a tabular dataset. For this, the river profile was linearized along its vector path, again extracted from OSM. The ''unrolled'' river was then divided into segments of a chosen length, typically 500 m, by defining a sequence of contiguous, nearly tangent circles whose centers lie along the river path, each separated by the chosen distance. Consequently, the straight-line distance between circle centers does not always match the segmentation step and is shorter in highly sinuous reaches. This is shown in the lower-right portion of Fig. 8, where five newly computed NDTI values are highlighted in red. The river profile was segmented using these circles, and for each segment, the mean NDTI was calculated and stored in a table. The two river margins and the river path, both from OSM, are shown in an inset of Fig. 13 at the confluence of a major tributary.

The circular shape was chosen for segmentation because its adirectional nature allows flow direction to be ignored, as if the circles were lenses to observe the river. Though not perfect, it provides a robust way to linearize the irregular two-dimensional river profile. A limitation occurs in narrow bends, where circles and their calculation areas overlap. The algorithm limits this by adaptively reducing circle radii to one-half or one-quarter of the predefined size, thereby decreasing overlap. This is done sparingly, since GEE processing time per circle (1–2 minutes) does not depend on circle size, and minimizing execution time requires keeping the number of circles low. With the adaptive strategy, average overlap between consecutive processing areas is about 2%, occasionally reaching 20%. A worst-case example for the fixed-radius mode is shown in Fig. 10, where the highly sinuous reach causes an unacceptably short straight-line distance between the centers of circles a.2 and a.3. Although the adaptive strategy improves performance between circles b.2 and b.3, the author has already proposed a more advanced algorithm to remove overlaps entirely. A key advantage of the current method, however, is complete river-surface coverage. Before returning mean NDTI values for each segment, the algorithm normalizes results to account for reduced-radius circles, as in Fig. 10b. This radius reduction (by factors of 2 or 4) also ensures proper alignment of the output data.

This phase produces a structured table with mean NDTI, NDWI, and NDVI values (and potentially additional indices), plus other statistical descriptors, ready for further processing and visualization. Each record also includes algorithm parameters and detailed georeferenced information—such as progressive distances, circle centers, tangent locations, and the full profile of each computed surface—ensuring complete traceability and reproducibility of the workflow and enabling robust reconstruction of all operations.

D. POST-PROCESSING PHASE

In post-processing, results are refined, integrated, and compared to add interpretive value and turn raw outputs into actionable information. Generated maps are typically enriched with study-specific datasets. For example, in flood analyzes, municipalities may overlay architectural and cadastral data to estimate damages, while topographic attributes (e.g., road width and slope) help Civil Protection agencies plan evacuation routes and ensure access for emergency vehicles.

Overlaying raster and vector data on a single map enables rapid visual validation and can reveal issues missed earlier, such as false positives. Fig. 9 shows an example from this study: the investigated river at its confluence with a turbid tributary, where the impact on turbidity is substantial. The resulting composite image integrates all data sources in a contextualized framework to support comprehensive interpretation.

Graphical representations also enable comparisons across layers, times, locations, and scales. Animations and plots often provide the clearest visualizations, as discussed in the

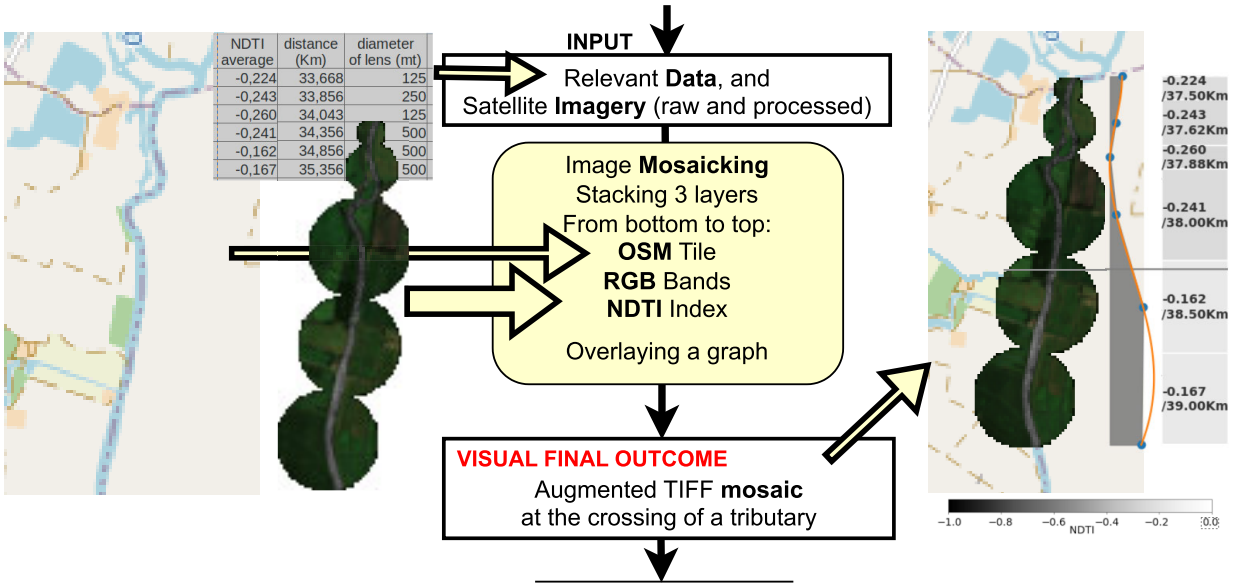

FIGURE 9. The Post Processing Phase: how to integrate diversified data to obtain a meaningful georeferenced result.

next section. Although some satellite platforms offer such tools, researchers frequently use external software.

An effective framework for managing this remote sensing workflow should also include a user interface that allows users to set the spatial extent, time range, quality thresholds, and output specifications through a dedicated control panel.

V. EXPERIMENTAL EVALUATION

This section reports results from satellite imagery processed with custom code executed for many hours on a cloud platform. The technological components represent a major part of the work. Particular effort went into visualizing the extracted information with maps and charts to clarify the results. The findings are mainly empirical and require further elaboration and validation in future studies.

The project uses Google Earth Engine (GEE), a planetary-scale platform for Earth science data and analysis that combines a multi-petabyte catalog of satellite images and geospatial datasets with large-scale analytical tools. GEE was selected for its free, unlimited research license and has proven well suited to this study. Analyzes are run via Python scripts. The GEE API is accessed in Jupyter Notebooks using geemap,[4] a package for interactive geospatial analysis and visualization with GEE. Graphical rendering uses the matplotlib[5] library, supported by dedicated Python routines.

This use case examines turbidity in a river reach, a multi-dimensional domain explored along three axes: space, time, and turbidity.

Spatially, the Mincio River reach upstream of Lake Mantua was simplified with a dedicated algorithm (see Pipeline section) into a 44 km linear span, then divided into 500 m sections. Temporally, the river was observed over one year,

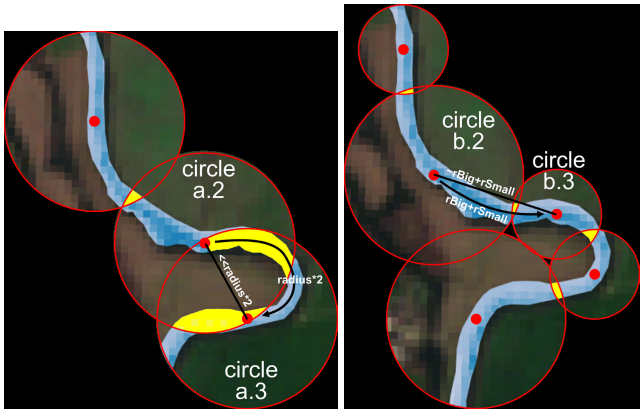

(a) Fixed radius mode (250 mt) (b) Adaptive (250 and 125 mt)

FIGURE 10. Reduction of defects (overlapping yellow areas) by using observation lenses that adapt to the sinuosity of the river, in a narrow bend of Mincio. The river surface shows NDWI pixels.

using one day per month, revealing clear contrasts between the cultivation (warm) and inactive (cold) seasons.

Turbidity was computed by applying the NDTI remote sensing index to each river section. Marked, abrupt turbidity spikes appeared at key locations and were highlighted in the charts to support interpretation of their causes; some were analyzed in greater depth. These increases typically decayed, often returning to pre-disturbance levels (recovery). The charts characterize these recovery events—especially their spatial extent and intensity—which vary widely, helping to illustrate the river's apparent self-purifying capacity.

A. DATASETS

The GEE platform provides access to thousands of datasets, each containing up to tens of thousands of terrestrial satellite images acquired over decades. Dataset lists are available in

[4]Geemap Python Library for GEE: https://geemap.org/
[5]Matplotlib, Visualization with Python: https://matplotlib.org/

the Earth Engine Data Catalog,[6] the official public repository, and in other online open-source catalogs maintained by expert communities.[7] Following the previously described Pipeline, these catalogs were examined to identify datasets covering the study area and meeting the required quality standards.

Two raster datasets imaging the Po Valley were examined: U.S. Landsat and European Copernicus (Sentinel), selected for their global coverage (Copernicus excludes polar regions), relevance, long-term continuity, and many spectral bands suitable for indices such as the NDTI. The "USGS Landsat 8 Collection 2 Tier 1 TOA Reflectance" dataset (since 2013) was considered but ultimately discarded in favor of the "Harmonized Sentinel-2 MSI: MultiSpectral Instrument, Level-2A" dataset (since 2017). If needed, older imagery is available, with Landsat extending back to the 1980s. Copernicus offers finer detail, with some bands at 10 m GSD versus Landsat's 30 m, crucial for a narrow river like the Mincio. While exact revisit intervals are approximate, Landsat images the river about 50 times per year (8-day RI), and Copernicus about 150 times per year (every 2–3 days), enabling more frequent cloud-free acquisitions.

To focus the analysis on the target river reach, georeferenced vector datasets of observed objects were used for accurate identification in the imagery. For this case study, freshwater river traces were needed. The SWOT River Database (SWORD),[8] a river-specific version of the SWOT dataset, was initially considered for its convenient integration in GEE, but tests showed it only roughly followed the Mincio course (Fig. 5).

The OpenStreetMap (OSM) database[9] was used for its accurate vectorized river geometry, including meanders. It provides riverbank vectors—used to delimit the surface for NDTI calculations—and the river axis, allowing river linearization, segmentation, and spatial averaging. As OSM is not accessible via GEE APIs, it was integrated through the geemap library.

Given the spatial and temporal constraints, multiple datasets were combined, leveraging the specific strengths of each.

B. EVALUATION METRICS

Turbidity measures how much suspended particles reduce water transparency and is widely used to monitor water quality and aquatic ecosystem health. This study uses a classical remote sensing index derived from satellite spectral bands for this purpose: the Normalized Difference Turbidity Index (NDTI):

$$NDTI = \frac{\text{red band} - \text{green band}}{\text{red band} + \text{green band}} \tag{1}$$

As explained by [27], in pure water, reflectance is weak in the green band (below 10%) and very low in the red band. As turbidity increases and suspended particles grow, red reflectance surpasses green. NDTI uses this spectral behavior of turbid water to detect turbid pixels.

Like any normalized difference index, NDTI is dimensionless and ranges from $[-1, +1]$, with higher values indicating greater turbidity. Here, it is computed along the 44 km northern reach of the Mincio River to identify sections and

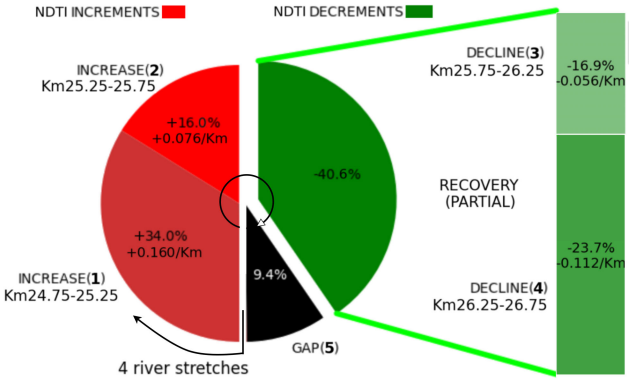

FIGURE 11. An NDTI peak with a partial RECOVERY, as measured in Corte Merlesco on 02-02-2024, shown with the specific metrics.

times with extreme turbidity. In the rest of this article, NDTI and turbidity are used interchangeably due to their close correspondence. Additional metrics introduced in this study are described below.

The availability of NDTI values also made it possible to examine their variations along the river course; this study identified roughly ten significant changes. To facilitate the understanding of these dynamics, specific definitions are introduced:

- JUMP (protrusion) = an intense change in turbidity experienced by the water between measurement points.
- BASELINE = the turbidity value before the disturbance.
- RECOVERY (bounce back) = the return of turbidity to its pre-disturbance value (its baseline).
- GAP = the percentage of NDTI variation not recovered.

To quantify these dynamics, a specific speed metric has been defined:

$$NDTI_s = \frac{\Delta NDTI}{\Delta s} \quad \left[\text{km}^{-1}\right] \tag{2}$$

where $NDTI_s$ represents the rate of NDTI variation as a function of the spatial distance Δs, in terms of velocity. The graph in Fig. 11 graphically shows how the turbidity increases and then decreases in one of the NDTI peaks analyzed. In this case turbidity remained significantly higher than the BASELINE where the perturbation began, as reported by the black GAP(**5**) slice. The 4 measurements range from (**1**) to (**4**) and concern consecutive stretches of the river each 500 metres long, reported clockwise, starting from the bottom. The pie chart shows the progression of the 4 fluctuations (red increments followed by green decrements) along space and their relative magnitude, also in terms of NDTI velocity

[6]GEE Data Catalog: https://developers.google.com/earth-engine/datasets
[7]GEE Community Catalog: https://gee-community-catalog.org/
[8]SWOT River DB: https://gee-community-catalog.org/projects/sword/
[9]Open Street Map free world map: https://www.openstreetmap.org/

expressed per kilometer. This NDTI disturbance has been circumscribed with the red balloon in the spatial plot reporting the entire river in Figure 14.

If high turbidity indicates poor water quality, rapid increases should reflect more severe disturbances. Conversely, sharp declines should signal strong self-purification, especially when a jump is fully offset by recovery.

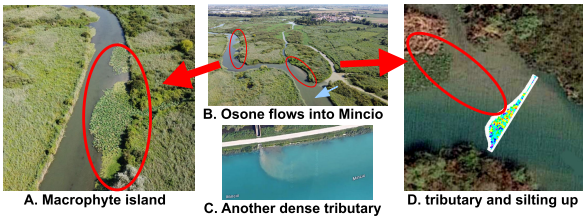

FIGURE 12. Significant locations inside the ROI for this Use Case. A,B,D: archive footage. C:Google Maps.

Jumps and their dynamics are shown in dedicated graphical outputs in the V-E4 section, which identify recoveries, gaps, and variation rates. Interpreting these metrics can guide investigation of natural or anthropogenic factors driving turbidity and its fluctuations.

C. USE CASES AND AREAS OF INTEREST

This study develops an automated tool to monitor river turbidity and its main variations. Rapid, intense turbidity increases are key to detect and quantify, as they may indicate point-source pollution. This phenomenon is common in many rivers, especially in highly anthropized areas where intensive human activity interacts with natural processes. Analyzing downstream conditions after such disturbances is also crucial to assess river resilience—its capacity to restore initial conditions, the speed and extent of recovery, and the conditions that influence its effectiveness.

In the examined case, highly turbid waters occur downstream of urban areas due to high loads of suspended solids and nutrients and very turbid tributaries such as the Osone, which drains intensively cultivated land. Its much lighter color than the Mincio, into which it flows, is clearly visible in Fig. 12. This particle load likely causes depositional sedimentation hazardous to navigation and accelerates riverbed infilling, as shown in the figure and hypothesized by a University of Parma research group [28].

The Osone, though a small tributary, is crucial to this study, which focuses on a long, narrow Area of Interest (AOI/ROI) along the upper Mincio River. The Mincio rises from Lake Garda, crosses the Po Valley, and feeds the three lakes of Mantua in Lombardy, Northern Italy.

The analyzed reach is about 44 km long. As detailed in the "Processing Pipeline" section, it is linearized with an algorithm that fits tangent circles, dividing the river into 500 m sections. These sections are used to calculate the NDTI index across seasons, yielding datasets of about 90 records—roughly twice the number of kilometers analyzed. The method is shown in Fig. 13, which includes two insets of the Osone confluence.

The preliminary results obtained from this study are described later in the V-E section.

D. EXPERIMENTAL METHODOLOGY

This research uses Copernicus satellite images to analyze turbidity and its variations in the Mincio River, a mid-sized river in the Po Valley. The study focuses on the upper course, from Lake Garda to the outskirts of Mantua. The dataset is three-dimensional: a 44 km spatial axis along the river with averages every 500 m; a temporal axis covering

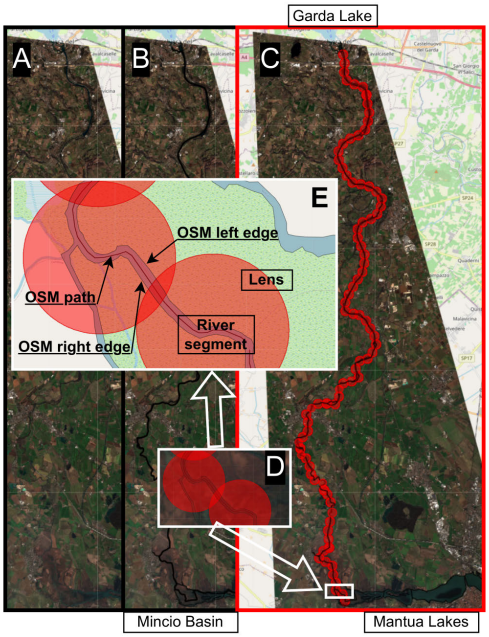

FIGURE 13. The ROI. A) RGB-only view. B) River edge overlay. C) Circular lenses used for NDTI measurements. D) Confluence of the Osone tributary into the Mincio. E) Confluence scaled up, with Open Street Map (OSM) algorithmic contributions, and results.

2024 - the most recent complete dataset available to date - with one clear-sky image per month, supplemented by partial 2023 data; and turbidity, estimated via the Normalized Difference Turbidity Index (NDTI). Under the observed conditions, NDTI values ranged continuously from -1 to about 0.

The working hypothesis is that turbidity in the upper Mincio is affected by agricultural activities, effluent from Lake Garda's wastewater treatment plant, and discharges from settlements along the river.

Observations, hypotheses, and conclusions were developed along the three dimensions (space, time, turbidity) and supported by space-centric, time-centric, turbidity-focused, and 3D visualizations. The 3D graphs were especially useful for overview and comparison.

To gain an initial understanding, the study began with spatial analysis. Turbidity was measured along the entire river course using a precise procedure described here. August was analyzed first as representative of summer,

when agricultural and livestock activities in the Mincio plain peak and their by-products, as suggested by several studies including Prof. Bartoli's group [29], are washed into watercourses. Turbidity can thus indicate this impact. The analysis was then repeated for February, representing winter, when such activities are largely halted. November was also examined, yielding expected intermediate results as expected. This initial analysis highlighted marked seasonal differences in turbidity and identified about ten locations along the river with substantial variations, which were mapped geographically - see figure 14.

Two previously identified segments were examined in more detail to assess temporal trends. Their limited length (a few kilometers) allowed analysis across all twelve months of 2024. The confluence of the Goldone canal with the Mincio was used as a case study. The Goldone drains agricultural runoff and is a tributary known for supplying large amounts of suspended solids to the Mincio. These tributaries appear light-colored in summer, as shown by earlier drone imagery. The analysis confirmed the strong seasonal trends previously observed and revealed two seasonal clusters—productive and quiescent—distinguished by clear differences in turbidity over the year.

To study turbidity in space and time, we used dedicated 3D plots. A 3D visualization of NDTI values was generated for the confluence with the Goldone in 2024, then extended to 2023 data and to the confluence with the Fossa Redone Superiore, another drainage canal, highlighting differences among the three cases.

The analysis concludes with plots that examine the main turbidity variations using the study's specific metrics (see Evaluation Metrics). These metrics characterize turbidity dynamics at six river points. Turbidity spikes were compared across sites and seasons to assess differences in intensity and variation rates, and to identify cases where a persistent gap remained—where the river did not fully recover its pre-disturbance state.

All data processing scripts were developed in Python 3.12.3, using the geemap library (v0.35.1) within Jupyter notebooks executed in the integrated Visual Studio Code environment (v1.104.1). Graphs were generated with matplotlib (v3.10.5) on a Linux Ubuntu 24.04.1 system in 2025. Data storage and exchange were managed using Microsoft Excel spreadsheets in the 2007–365.xlsx format.

E. RESULTS AND CRITICAL ANALYSIS

1) SPATIAL ANALYSIS

This analysis, summarized in graphs a–c in Figures 14 and 15, examines turbidity dynamics along the 44 km upper stretch of the Mincio River on two 2024 dates: February 2 (cold season) and August 8 (warm season). Turbidity is quantified with the standard remote sensing metric NDTI (Normalized Difference Turbidity Index) from satellite imagery. The plots use river length on the horizontal axis to show spatial variation, while time appears as a comparative factor between cold- and warm-season conditions. This setup identifies where turbidity peaks and where the steepest spatial changes occur; these locations are then selected for detailed temporal analyses. Seasonal data are color-coded blue (cold) and orange (warm), with orange chosen over red to improve visual accessibility, especially for visually impaired readers.

Graph 14 shows turbidity values. The upper horizontal axis reports river kilometers downstream from the Peschiera del Garda source. The vertical axis shows turbidity from -0.84 (very clear water near the source; green tick marks) to $+0.01$ (more turbid water; red tick marks). The two series are original values from 500 m raster segments. The lower horizontal axis shows the progressive measurement number (twice the distance in kilometers). Turbidity varies substantially, with a clear decline in transparency downstream: NDTI is about -0.45 at the source and approaches -0.15 farther downstream, with some seasonal variation.

In the cold season (blue), water from Lake Garda is initially very clear but becomes markedly turbid after 6 km, at the confluence with the Fossa Redone Superiore canal. Although variability persists, water quality does not return to initial levels. This reduced recovery in winter may be explained by the diminished phytodepurative activity [30] of aquatic vegetation, which is less active or less abundant during this period [31].

In the warm season (orange), the water is moderately clear at the source but quickly becomes turbid after 3 km, near Salionze, coinciding with the discharge from the Gardesana community wastewater treatment plant. Its impact appears more pronounced in summer, likely due to the substantial seasonal increase in tourism around Lake Garda.[10] The discharge from the Fossa Redone Superiore also contributes significantly during the summer. However, from that point downstream to the Mantua lakes, turbidity generally remains higher during the cold season, as highlighted by the comparative box plots at the bottom of the graph (labeled "Hot" and "Cold"), which are color-coded according to seasonal prevalence.

Graph 14b illustrates turbidity variations (rather than absolute values). The horizontal scale matches Graph 14a. Its purpose is to highlight the most intense spikes, i.e., points where turbidity shifts sharply. Bars diverge from a central baseline: upward bars indicate increasing turbidity, while downward bars mark decreases relative to the preceding 500-meter segment. Major fluctuations are labeled with local place names or GPS coordinates. The graphs in figure 14 share the color scheme, as the colors distinguish the seasons (blue for cold, orange for warm). In Graph 14b, gray bars represent the intermediate season (November 3rd). Bars are overlaid, not stacked, so extreme values emerge clearly at the tips of the bars.

Turbidity changes ranged from -0.138 to $+0.25$, except for one outlier ($+0.5$) truncated to avoid distorting the graph.

[10] +27% tourist arrivals from 2014 to 2024 in the 23 lakeside municipalities: https://www.legambientelombardia.it/wp-content/uploads/2025/07/0705-comunicato-overtourism-sul-Garda_II-appuntamento-veneto-GDL.pdf

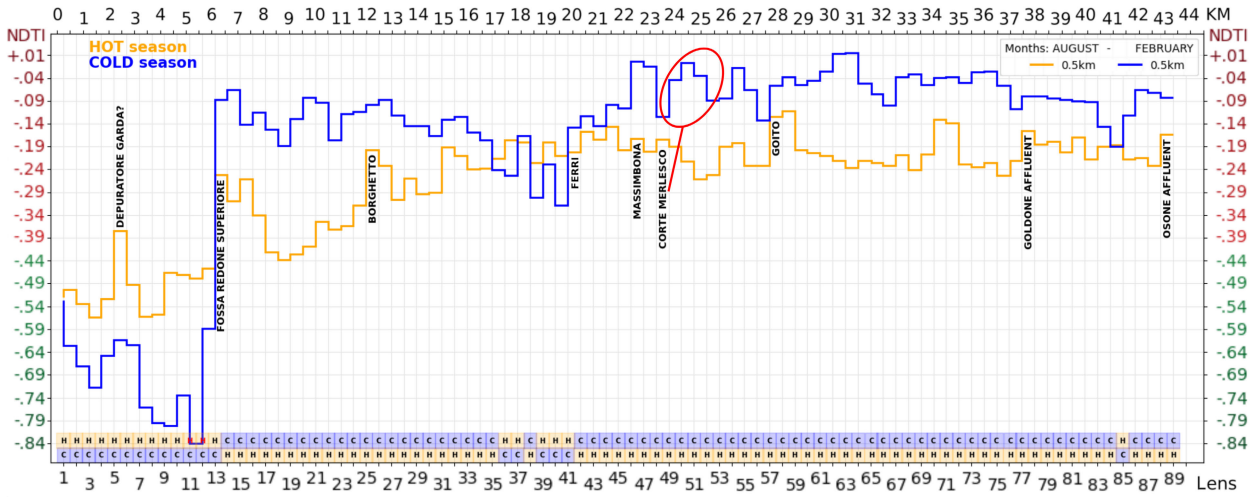

(a) NDTI VALUES on 500m segments (two seasons - turbidity increasing upwards) The red circled peak is depicted in Fig. 11. Among the reported locations (vertical texts) also appear the six peaks of the NDTI index examined in detail in the graph 20.

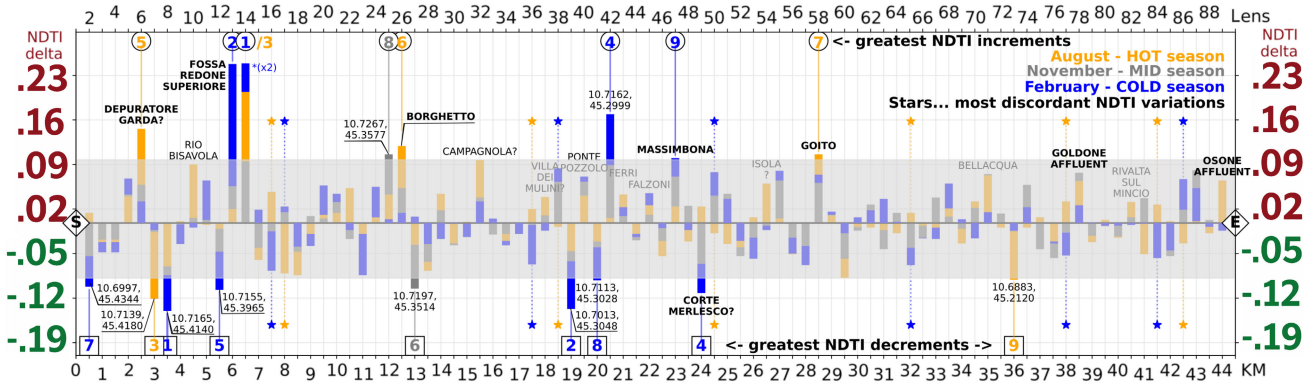

(b) NDTI VARIATIONS of 500 mt-long stretches - three seasons (UPWARDS bars in places that get THICKER, downwards -> cleaner)

(c) River Basin - High Mincio (from Garda Lake to Mantua) - OSM background, spots from GMaps or Sentinel-2 or drone

FIGURE 14. **Spatial Analysis - 2024 NDTI values and variations along the entire upper course of the Mincio river.**

A gray rectangle hides smaller bars and highlights major fluctuations, defined as those exceeding one-third of the maximum spike, yielding 18 prominent spikes (9 positive, 9 negative). Each spike is labeled with its name, ranked (1 = strongest), and marked with the season's color—circles for increases and boxes for decreases. Color segments within vertical bars enable quick comparison across three seasons and 88 river segments. The cold season showed the strongest variations (41 times), followed by the warm (29) and intermediate (18) seasons. Star markers indicate locations where seasonal trends diverge, with turbidity rising in one season and falling in another.

Graph 14c shows the upper Mincio study area on a geographic map, where datasets have been linearized to represent the river's course. Key locations of turbidity variation are marked and illustrated with aerial imagery, satellite orthophotos, or drone images, including the circular masks used by the remote sensing algorithm. Numbered labels match the critical positions in Graphs 14a and 14b. The map is rotated horizontally to align with these graphs.

Fig. 15 shows three heat maps. Graph 15a displays August 2024 turbidity values (500 m resolution) at increasing spatial aggregation levels, visually confirming the 500 m sampling choice. Turbidity clearly increases downstream, indicating

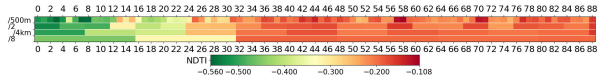

(a) NDTI Values - Spatial aggregations along the lenses (HOT season - August)

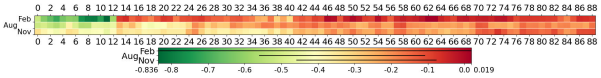

(b) NDTI Values - Seasonal comparison (February vs August vs November)

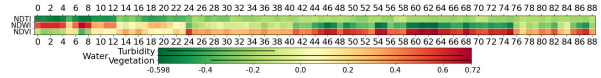

(c) NDTI, NDWI, NDVI Values - Remote Sensing indices comparison (Turbidity, Water, Vegetation) - August data

FIGURE 15. Spatial Analysis - Year 2024 data - Heat Maps - Aggregations, seasonal and indices comparisons.

accumulation of suspended particles. The two lines at the bottom (colored squares C and H) indicate the season of highest turbidity along each river reach.

Graph 15b compares NDTI values across the three seasons, confirming earlier observations. The accessory color bar below the graph, featuring black segment markers, facilitates interpretation.

Graph 15c compares turbidity data from August 2024 with values derived from two other popular remote sensing indices: NDWI (water) and NDVI (vegetation), extracted alongside NDTI. Unlike the previous graphs, color ranges differ because NDWI and NDVI vary more widely than NDTI, as indicated by their respective color bar segments. An inverse relationship is evident between NDWI and NDVI, as expected from their antithetical meanings. The data show an inverse relationship between NDTI and NDWI, meaning the water is less turbid in deeper reaches, presumably because debris have more space to disperse. A direct relationship is also apparent between NDTI and NDVI, meaning aquatic vegetation is more abundant where the water is more turbid, likely due to a greater availability of suspended nutrients. Importantly, the developed extraction algorithm schematically shown in Figure 16, is adaptable to compute any RS index, provided that the required spectral bands are available in the satellite imagery.

Conclusion. The waters flowing from Lake Garda (also known as Benaco) into the Mincio are objectively very clean, as evidenced by civil and industrial wastewater is collected by an extensive and efficient sewer system around the lake .[11] However, these substances eventually enter the river further downstream, along with substantial agricultural wastewater during the warm season. Up to 179 kg N/ha comes from livestock effluents[12] The Nitrogen loss in surface runoff is a severe side effect of the livestock industry [32]. This seasonal input significantly affects turbidity dynamics.

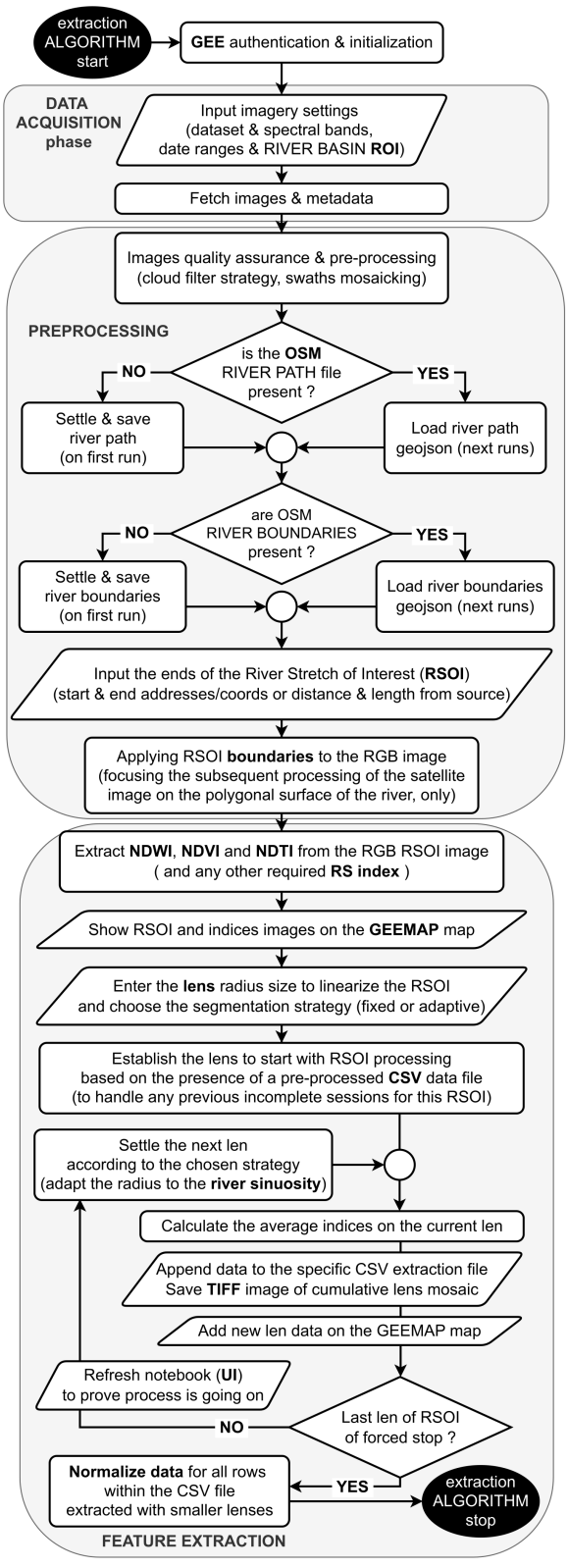

FIGURE 16. The indices extraction ALGORITHM - from raw satellite imagery to meaningful turbidity information - down the RS Pipeline.

[11] Benaco lake wastewater treatment: https://www.depurazionibenacensi.it/depuratore.asp

[12] Soil and agricultural systems monitoring plan (Piano di monitoraggio dei suoli e dei sistemi agricoli) - 2024: https://www.ersaf.lombardia.it/wp-content/uploads/2025/05/Rapporto-Monitoraggio_suoli_24_def.pdf.

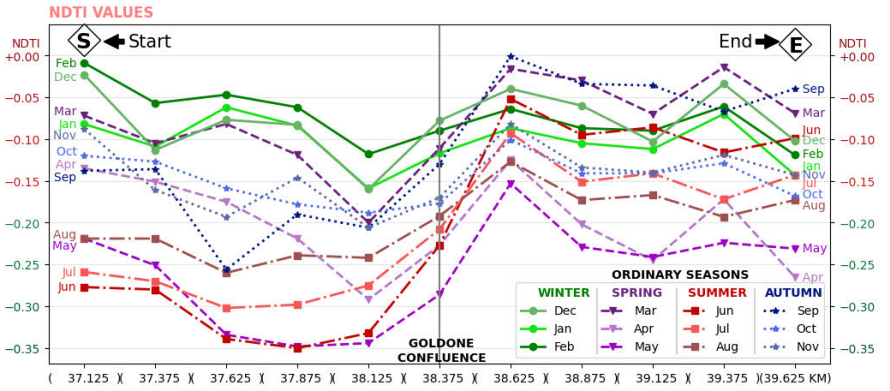

(a) Monthly TIME SERIES

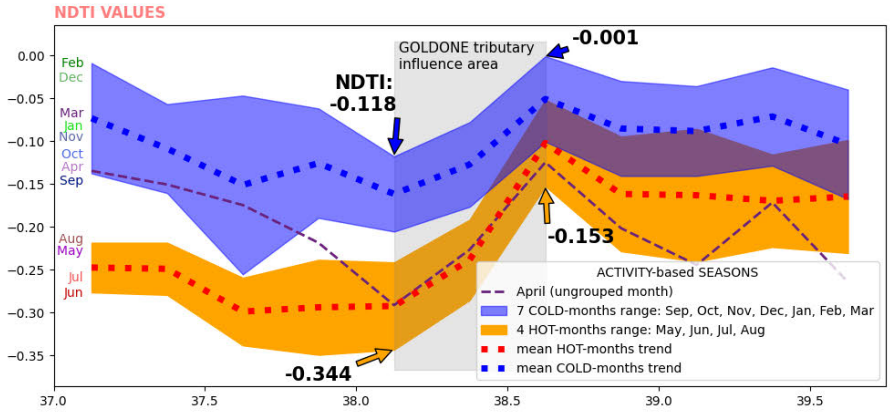

(b) Seasonal TRENDS

FIGURE 17. Temporal Analysis - Goldone/Mincio confluence - NDTI data along 3 Km stretch - year 2024.

2) TEMPORAL ANALYSIS

Graphs a–e in Fig. 17 and Fig. 18 emphasize the temporal dimension, showing turbidity index values and their variation along nearly three kilometers of the Mincio River centered on its confluence with the Goldone. This analysis uses a finer spatial resolution of 250 meters—half that of the previous spatial analysis—to allow more detailed observations. On the horizontal axis, brackets above the ticks schematically indicate the spatial extent of the eleven circular windows used to calculate the graphed values; kilometer marks show the distance of their centers from the river's source. The exact confluence is shown in gray: as a vertical line in Graph 17a and as a shaded area in Graph 17b. In the observed section (km 37.000–39.750), NDTI values range from –0.349 to –0.001, revealing marked temporal variability across the selected days in 2024. Higher NDTI values (marked in red on the vertical axes) correspond to more turbid waters. The same three-dimensional data domain used earlier is examined here through alternative two-dimensional views to aid interpretation, suggest hypotheses, and support conclusions. Particular attention was given to visualization choices for this specific dataset; for instance, the color scheme for months also distinguishes the four seasons, as shown in the legend of Graph 17a.

Graph 17a shows the temporal series and highlights months with stronger correlations. A faint seasonal trend appears more clearly in Graph 17b, which identifies two clusters: seven months in a ''cold period'' (blue band) and four in a ''warm period'' (orange band). April does not fit either group and is shown separately. The bands remain distinct, with their mean lines (dashed curves) consistently apart. These seasonal patterns likely reflect different natural dynamics and human activities along the river in the two periods. The tributary's effect is evident, as it consistently increases turbidity in all twelve months. Winter waters are overall more turbid, confirming the spatial analysis. Graph 17b also shows that turbidity at the end of the reaches tends to return to its initial levels. This ''recovery effect,'' described in the metrics section, is weaker in summer and merits further investigation.

In Graph 17a, the gentler slope of the twelve monthly curves at the confluence shows that turbidity variations in winter are about half as strong, as indicated by the four highlighted arrows. This supports the hypothesis that the tributary carries less suspended sediment when agricultural activity is reduced. However, the strong overlap of the monthly curves makes the graph hard to interpret, so the subsequent graphs are needed. Later, three-dimensional plots will also allow comparisons across years and locations.

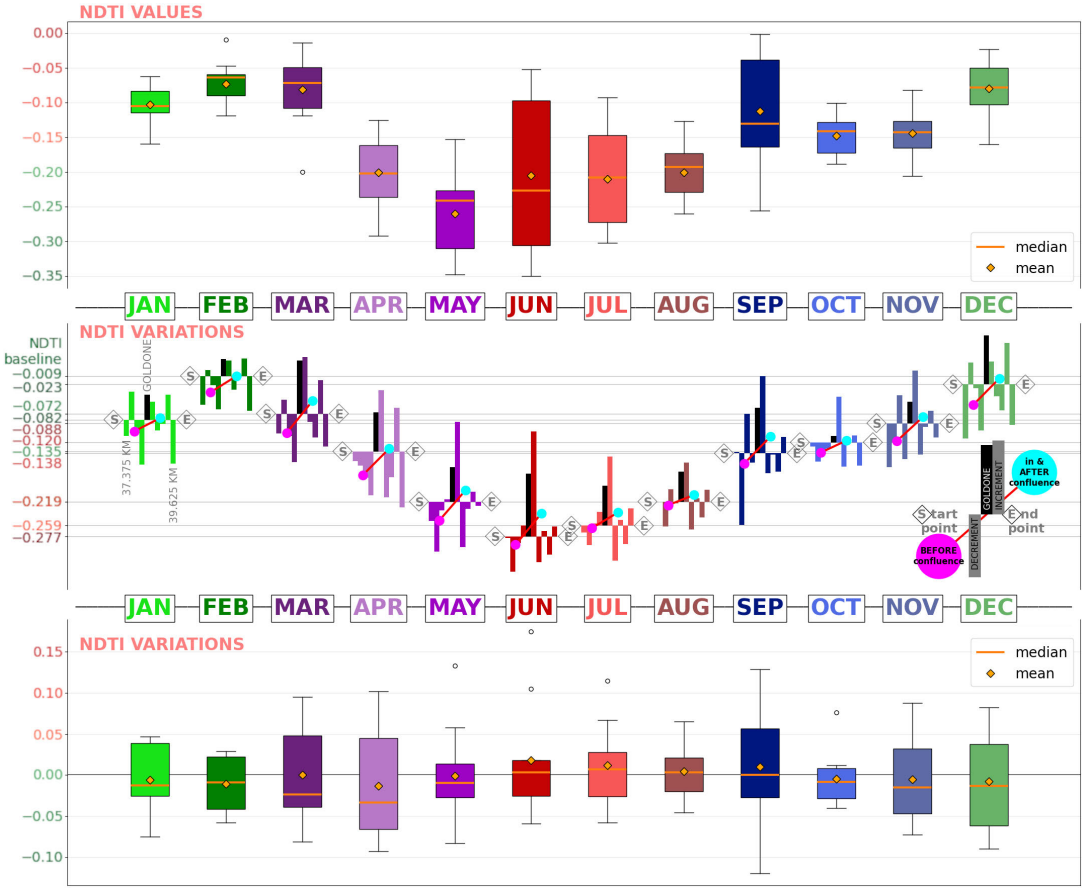

FIGURE 18. At the top: Monthly Excursions (along 3 Km centered stretch at the Mincio-Goldone confluence). In the middle: Monthly Increments/Decrements (drawn over each month's baseline at Km 37.125) At the bottom: Monthly Variations.

The graphs in Fig. 18 sharpen the temporal focus, showing twelve-month patterns at eleven equidistant sampling points along the 3 km reach. The horizontal axis separates months, avoiding the overlapping lines in Graph 17a. Conceptually, it is as if an observer traveled the reach once a month, drifting with the current and recording turbidity. This layout clarifies temporal variation. Graph 18.top shows monthly turbidity values; Graphs 18.middle and 18.bottom show their variation across the eleven points (2.75 km). The monthly color scheme matches Graphs 17a and 17b. Bars above the axis midpoint indicate high or increasing turbidity; those below indicate low or decreasing turbidity.

These three graphs highlight the largest absolute values and variations, showing when and where the steepest increases or decreases occurred. For each month, the box-and-whisker plots in Graphs 18.top and 18.bottom summarize the NDTI data, values, and variations, including the median, mean, and outliers. In contrast, Graph 18.middle uses histograms to show spatial variation across the eleven segments of the reach. Extended turbidity variations over longer sections appear where adjacent bars show similar patterns. In both Graphs 18.top and 18.middle, the vertical scale of turbidity is consistent, so that when examined sequentially, the monthly data form an undulatory pattern: they are higher in winter and lower in summer. This finding confirms what was already suggested by the spatial analysis; however, it is demonstrated here as a consistent trend without discontinuities.

This analysis examines the Goldone tributary's impact on turbidity. In Graph 18.middle, bars for the tributary outlet are shown in black each month. Each histogram includes paired circles—cyan downstream and magenta upstream—representing average NDTI variation in each sub-reach. Red line segments connecting the circles across months show spatial turbidity differences. Their slopes are consistently positive, indicating higher turbidity downstream in all months, with stronger contrasts from March to June and again in September, November, and December, when pre- and post-confluence turbidity differ most.

3) COMPREHENSIVE GRAPHS

The 3D graphs presented here, a–c in Fig. 19, aim to replicate the three-dimensional structure of the dataset under study: along the X-axis is the river course, along the Y-axis is time (in months), and along the Z-axis are the NDTI values (turbidity). The twelve bars represent the changes in turbidity along the study reach over the twelve months. The confluence with the Goldone is depicted in Graph 19a, based on 2024 data, and in Graph 19b, based on 2023 data. Graph 19c

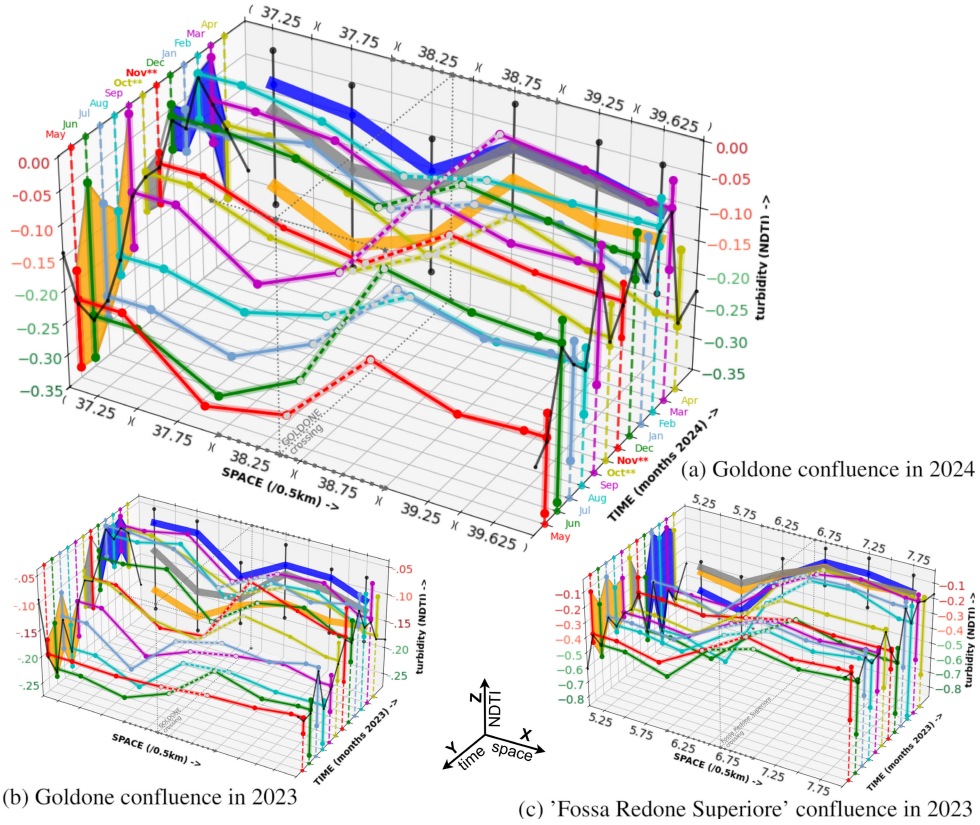

FIGURE 19. 3D Comprehensive Graphs - Space, Time and NDTI (values and excursions) on two major tributaries.

shows the confluence with the "Fossa Redone Superiore" canal in 2023. The three-dimensional visualization facilitates comparisons across different locations and years.

Along the X-axis, bars show mean NDTI over 500-meter segments, giving six measurements per month and 72 total points. Because many bars overlap, months are reordered to start in May, emphasizing the lower summer block. To reduce visual clutter, the 3D graphs use six distinct colors repeated across the twelve months. Points at the tributary outlet are highlighted on four horizontal planes and connecting edges with dark dashed lines, while corresponding turbidity segments on the bars are marked with white dashed lines. These mark the steepest slopes, confirming abrupt turbidity shifts from the Goldone inflow. In all graphs, turbidity increases upward: reddish ticks on the vertical axis indicate higher NDTI (more turbid water), and green ticks indicate lower NDTI (clearer water).

The two YZ planes show additional information: turbidity excursions in twelve vertical segments, which project monthly NDTI values from the bars to both sides. Their height indicates monthly variation. Colored regions on the rear-left plane connect these excursion bars, highlighting the earlier seasonal clusters—orange for the warm season, blue for the cold season, and gray for the transitional period.

On the rear-right plane, turbidity excursions are shown in a transverse view, projecting measurements from the six observation windows over the twelve months. This 3D dual perspective enhances interpretation. The rear-right plane also displays median seasonal lines—the three colored bands (orange, gray, blue) that confirm the dynamics seen in Graph 19a. In 2023, these bands are clearly separated; in 2024, the cold and transitional bands partly overlap.

Beyond representing the study area's spatial structure, the 3D graphs compactly display the dataset and reveal insights that confirm or refine the 2D analyses. For example, the 2023 Goldone confluence graph clearly supported reclassifying September into the warm cluster and shifting October and November toward the cold group. This was possible because, unlike 2D views, the 3D layout places sequential turbidity changes side by side with less overlap, and their projections onto the planes provide strong interpretive leverage. For the Goldone confluence in 2024, however, the seasonal assignment of these months is less clear.

Graph 19c, showing 2023 data for a different location—the confluence with the "Fossa Redone Superiore"—suggests further observations. The twelve bars exhibit much greater uniformity, with less temporal variability than in the two Goldone graphs. This is confirmed by the three seasonal bands in the background, which overlap substantially. Only the blue band diverges, and only in the initial segment, a pattern corroborated by the excursion traces projected on the rear-left plane, which indicate greater NDTI variability during the cold season. The black polyline drawn on the left

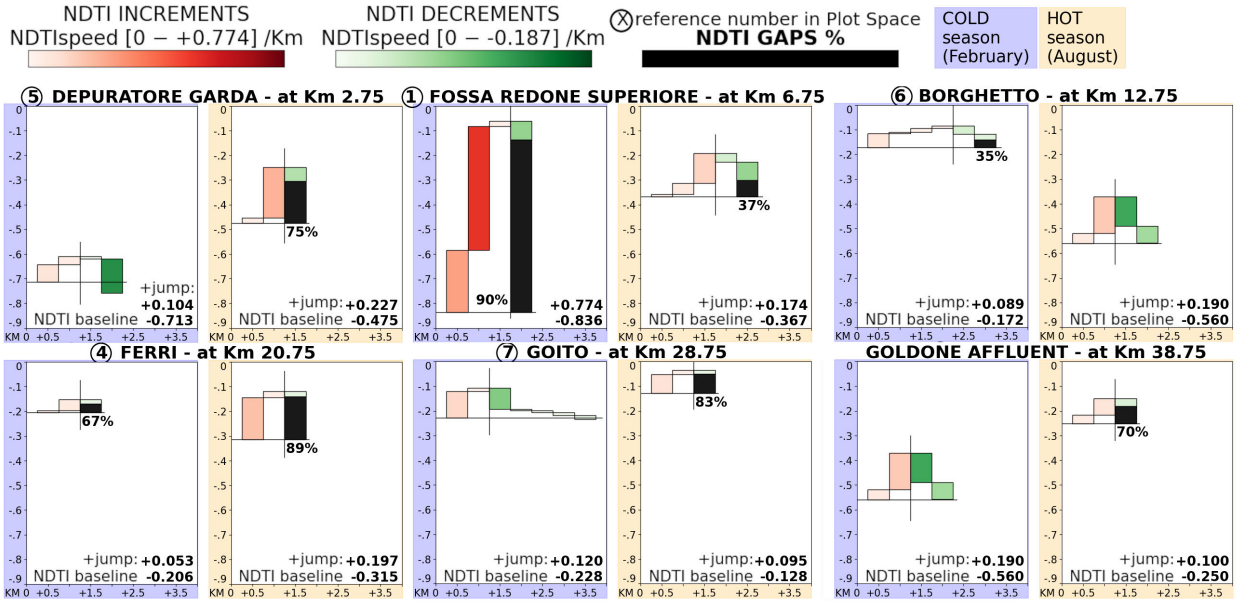

FIGURE 20. SPIKE FOCUSED PLOTS - The Six Most Intense NDTI Spikes along the Mincio - year 2024. NDTI metrics described in section V-B. Locations reported in Figure 14.

rear plane connecting the NDTI values calculated at the initial point of the studied stretch of the river, in the various months (along the Y-axis) further distinguishes the two sites. In the Fossa graph, this polyline consistently lies at the base of the three colored surfaces (orange, gray and blue), indicating that turbidity starts low and rises steadily along the reach in all months. In contrast, at the Goldone confluence, the black polyline remains low during the warm season (orange area) but shifts upward during the cold season (blue area) in both 2023 and 2024. This confirms that turbidity begins low and increases in summer, whereas in winter it starts high from the outset.

4) ANALYSIS OF TURBIDITY SPIKES

The graphs in Fig. 20 analyze intense turbidity spikes—points along the river with strong turbidity perturbations. Six notable spikes are reported, selected as the strongest from the previous spatial analysis. Each is examined in both seasons, yielding twelve visualizations. The graphs detail each spike's seasonal behavior, spatial extent, recovery speed (return to baseline turbidity), and restoration magnitude. Original metrics used to quantify these patterns are described in Section V-B.

The graphs show recovery after each spike, but with varying completeness. If higher turbidity suggests potential pollution, the subsequent return to clarity reflects natural remediation; thus, the intensity and spatio-temporal pattern of recovery are key. Each graph aligns the rise and fall of turbidity along the distance axis to assess river resilience.

Each peak is labeled with a circled number, matching the numbering in the spatial analysis graph 14b and indicating the most common causes of turbidity variation. Three locations (4, 6, 7) reflect disturbances from inhabited centers. The others show the effects of very turbid inputs from the three most impactful tributaries: the Garda sewage treatment plant (label 5), described in Section V-E1, and the two small rivers Goldone and Fossa Redone (label 1), discussed in Section V-E3. For each location, summer (ochre) and winter (light blue) graphs are shown side by side. Bar charts indicate each river segment's contribution to the spike relative to total turbidity variation. All twelve spikes share a uniform intensity scale for comparison. Each graph reports the baseline NDTI and spike magnitude at its base.

The rate of change per kilometer during each spike's rise and fall is shown by the color scale at the top: red for increases and green for decreases, with stronger colors indicating faster NDTI changes. Incomplete recoveries are marked by a black final bar labeled with the unrecovered percentage ("gap").

Eight of the twelve cases show a gap, often large and sometimes moderate (30%). The clearest case is the Fossa canal confluence: in winter the spike is strong (NDTI +0.774) but only 10% of the lost clarity returns, whereas in summer the spike is smaller (+0.174) and recovery is much greater. This sharp seasonal contrast merits further study. Spike characteristics differ greatly by season at each site. The six sites are ordered by distance from the river source, but this ordering does not appear to influence spike behavior.

F. LIMITATIONS

As with many remote sensing studies, this research faces technical and methodological limitations. This section outlines the main challenges encountered; some have been resolved, while others remain only partially addressed.

During image acquisition, the need for a dataset resolving fine-scale details of a narrow river like the Mincio became evident. Thus, the Copernicus platform was chosen over Landsat, as discussed in the processing pipeline section.

However, the 10 m^2 minimum analysis area still limits spatial refinement.

Temporal constraints also affect this study. Although the analyses presented here yielded significant insights, they are limited to a single year of observations. Expanding the temporal window is needed to strengthen the findings and enable long-term comparisons. Further assessment may also support replacing daily measurements with monthly averages to reduce the influence of transient anomalies.

The pre-processing phase has an additional limitation: it does not account for bridges and dams along the river. These structures, clearly visible in satellite imagery, artificially raise NDTI values within affected observation windows. Because bridges are often near populated areas, they further amplify the NDTI spikes already caused by urban discharges. This contamination of the results occurs because the OSM dataset used in this study rarely filters out regions occupied by such structures, as it is the specific version dedicated to watercourses. By integrating a cartographic dataset into the focusing algorithm, it will be possible to obtain a refined solution that excludes unwanted surfaces from the index calculation.

Further assessment of the model's limitations and possible refinements could come from collaboration with domain experts, whose in-situ measurements and photographic documentation would help validate and verify the ongoing research.

VI. CONCLUSION

This project analyzes surface water bodies, which play a fundamental role in providing ecosystem services but are increasingly threatened by unsustainable agro-industrial practices. Although it focuses on a short period, the system demonstrates that it is possible to assess the condition of a waterway by analyzing trends and fluctuations in water turbidity along its course. By providing significant information on a medium-sized river in the Po basin affected by eutrophication phenomena, the tool allows us to identify some of the impacts to which it is subject. This is due to three specific analyses focused respectively on space, time and the way in which the observed phenomena occur, which are discussed in detail in section V-E. Analysis of the NDTI index in the long stretch of the river involved allowed for the precise identification of numerous points with significant peaks in turbidity, located near residential areas or at the confluence with agricultural, livestock or civil wastewater channels. By adding the time factor, the study allows us to better contextualize the extent of the fluctuations, arriving at the hypothesis of reasonable relationships with the human activities carried out in the area, also considering seasonal factors, which also have their weight. The study, which examines the shape of the identified turbidity peaks, shows how quickly they reach their apex, and how well the river is able to neutralize them, revealing different patterns in various cases, also depending on the different seasons in which they occur. The findings and conjectures are supported by outputs such as maps, graphs and data tables obtained through an efficient processing pipeline, including unique 3D plots.

The project developed an open-source, cloud-based remote sensing tool to support this analysis. Its use extends beyond the Mincio River; by integrating higher-resolution satellite datasets, it could be applied to narrower channels and tributaries, such as the Goldone and Osone streams, which are only 10 meters wide. This would enable tracing point-source pollution responsible for the turbidity peaks reported in this study, potentially including finer sources like the one shown in Fig. 12. The approach could also be applied to other rivers facing similar environmental challenges; a preliminary test on the nearby Oglio River has already produced promising results.

The turbidity analysis framework developed here could be extended to detect abnormal vegetative islands or sediment accumulation—examples in Fig. 12—which can significantly hinder navigation and water flow. This would involve integrating the NDTI index with vegetation and water indices (NDVI, NDWI), already produced in the current version (Fig. 15).

This research could be extended to explore other correlations. For instance, the fluctuations reported in the Analysis of Turbidity Spikes section could be cross-referenced with rainfall, river meandering, and flow velocity to assess their impact on turbidity variability.

Although the model is optimized for riverine ecosystems, it could be adapted to lakes, but their larger spatial extent would require substantial changes to the framework.

REFERENCES

[1] J. Burkholder, B. Libra, P. Weyer, S. Heathcote, D. Kolpin, P. S. Thorne, and M. Wichman, "Impacts of waste from concentrated animal feeding operations on water quality," *Environ. Health Perspect.*, vol. 115, no. 2, pp. 308–312, Feb. 2007.

[2] N. Jersak-Cosmann, S. C. Sampaio, F. G. da S. Pinto, D. Palma, J. Dieter, M. Claudia, S. Cordovil, and A. de Varennes, "Transport of nutrients and bacteria in runoff after the application of swine wastewater," in *Proc. Int. J. Food, Agricult. Environ. (JFAE)*, 2012, vol. 10, no. 2, pp. 255–261. [Online]. Available: https://api.semanticscholar.org/CorpusID:97125551

[3] A. F. Doblinski, S. C. Sampaio, V. R. D. Silva, L. H. P. Nóbrega, S. D. Gomes, and T. C. Dal Bosco, "Nonpoint source pollution by swine farming wastewater in bean crop," *Revista Brasileira de Engenharia Agrícola e Ambiental*, vol. 14, no. 1, pp. 87–93, Jan. 2010.

[4] E. Commission. (2023). *Waste Framework Directive*. [Online]. Available: https://environment.ec.europa.eu/topics/waste-and-recycling/waste-framework-directiveen

[5] J. A. R. de Souza, D. A. Moreira, R. O. Batista, J. A. O. Saraz, and O. L. Z. Marín, "Chemical alterations in soils fertirrigated with wastewater from swine facilities," *Revista Colombiana de Ciencias Pecuarias*, vol. 25, no. 3, pp. 360–368, Sep. 2012.

[6] L. Gianquintieri, D. Oxoli, E. G. Caiani, and M. A. Brovelli, "Implementation of a GEOAI model to assess the impact of agricultural land on the spatial distribution of $PM_{2.5}$ concentration," *Chemosphere*, vol. 352, Mar. 2024, Art. no. 141438.

[7] M. Pinto, R. L. Cruz, E. P. Frigo, M. S. Frigo, and E. Hermes, "Nitrogen groundwater contamination consequential of irrigation with effluent from sewage treatment," *IRRIGA*, vol. 18, no. 2, pp. 270–281, 2013.

[8] S.-H. Kim, D.-H. Lee, M.-S. Kim, H.-P. Rhee, J. Hur, and K.-H. Shin, "Systematic tracing of nitrate sources in a complex river catchment: An integrated approach using stable isotopes and hydrological models," *Water Res.*, vol. 235, May 2023, Art. no. 119755.

[9] D. D. Hill, W. E. Owens, and P. B. Tchounwou, "Impact of animal waste application on runoff water quality in field experimental plots," *Int. J. Environ. Res. Public Health*, vol. 2, no. 2, pp. 314–321, Aug. 2005.

[10] M. Uzun, "Analysis of manyas lake surface area and shoreline change over various periods with DSAS tool," *Turkish J. Remote Sens.*, vol. 6, pp. 35–56, Apr. 2024.

[11] J. Luo, R. Pu, H. Duan, R. Ma, Z. Mao, Y. Zeng, L. Huang, and Q. Xiao, "Evaluating the influences of harvesting activity and eutrophication on loss of aquatic vegetations in Taihu lake, China," *Int. J. Appl. Earth Observ. Geoinf.*, vol. 87, May 2020, Art. no. 102038. [Online]. Available: https://www.sciencedirect.com/science/article/pii/S0303243419304921

[12] Z. Zhu, X. Li, Q. Bu, Q. Yan, L. Wen, X. Chen, X. Li, M. Yan, L. Jiang, G. Chen, S. Li, X. Gao, G. Zeng, and J. Liang, "Landwater transport and sources of nitrogen pollution affecting the structure and function of riverine microbial communities," *Environ. Sci. Technol.*, vol. 57, no. 7, pp. 2726–2738, Nov. 2023.

[13] D. Malferrari, A. Laurora, M. F. Brigatti, M. Coltorti, D. Di Giuseppe, B. Faccini, E. Passaglia, and M. G. Vezzalini, "Open-field experimentation of an innovative and integrated zeolitite cycle: Project definition and material characterization," *Rendiconti Lincei*, vol. 24, no. 2, pp. 141–150, Jun. 2013.

[14] E. Tullo, A. Finzi, and M. Guarino, "Review: Environmental impact of livestock farming and precision livestock farming as a mitigation strategy," *Sci. Total Environ.*, vol. 650, pp. 2751–2760, Feb. 2019. [Online]. Available: https://www.sciencedirect.com/science/article/pii/S0048969718338919

[15] F. Bautista, Y. Aguilar, and E. Díaz-Pereira, "Soils as natural reactors for swine wastewater treatment," *Tropical Subtropical Agroecosystems*, vol. 13, pp. 199–210, Jan. 2011.

[16] G. Triboli, M. Picone, and M. Bertogna, "Intelligent livestock waste sensing & management: Architecture and challenges in the po valley," in *Proc. IEEE Symp. Comput. Commun. (ISCC)*, Jun. 2024, pp. 1–6.

[17] G. Triboli, M. Picone, and M. Bertogna, "Integrating IoT and simulation for efficient livestock waste spread in the po valley," in *Proc. 28th Int. Symp. Distrib. Simul. Real Time Appl. (DS-RT)*, Oct. 2024, pp. 144–145.

[18] N. Asproulis, "(Safe) water as the condition for sustainable development in light of the climate crisis: An eastern orthodox reflection," *Religions*, vol. 15, no. 11, p. 1326, Oct. 2024.

[19] Á. Vári, S. A. Podschun, T. Erős, T. Hein, B. Pataki, I.-C. Ioja, C. M. Adamescu, A. Gerhardt, T. Gruber, A. Dedić, M. Ciric, B. Gavrilović, and A. Báldi, "Freshwater systems and ecosystem services: Challenges and chances for cross-fertilization of disciplines," *Ambio*, vol. 51, no. 1, pp. 135–151, Jan. 2022.

[20] J. Xue and B. Su, "Significant remote sensing vegetation indices: A review of developments and applications," *J. Sensors*, vol. 2017, pp. 1–17, May 2017.

[21] J. Yan and L. Wang, "Suitability evaluation for products generation from multisource remote sensing data," *Remote Sens.*, vol. 8, no. 12, p. 995, Dec. 2016.

[22] C. Sun, J. Li, L. Cao, Y. Liu, S. Jin, and B. Zhao, "Evaluation of vegetation index-based curve fitting models for accurate classification of salt Marsh vegetation using sentinel-2 time-series," *Sensors*, vol. 20, no. 19, p. 5551, Sep. 2020. [Online]. Available: https://www.mdpi.com/1424-8220/20/19/5551

[23] A. Latwal, S. Rehana, and K. S. Rajan, "Spatiotemporal analysis of turbidity in tropical reservoirs using sentinel-2 satellite imagery under catchment dynamics," *Remote Sens. Applications: Soc. Environ.*, vol. 39, Aug. 2025, Art. no. 101631. [Online]. Available: https://www.sciencedirect.com/science/article/pii/S2352938525001843

[24] P. Abel Nugraha Ardyan and Redondo, "Water turbidity qualitative analysis based on sentinel imagery in jeneberang river downstream, makassar, south sulawesi," *IOP Conf., Earth Environ. Sci.*, vol. 1525, no. 1, Jul. 2025, Art. no. 012028, doi: 10.1088/1755-1315/1525/1/012028.

[25] A. Baltodano, A. Agramont, I. Reusen, and A. van Griensven, "Land cover change and water quality: How remote sensing can help understand driver-impact relations in the lake Titicaca Basin," *Water*, vol. 14, no. 7, p. 2733, 2022. [Online]. Available: https://www.mdpi.com/2073-4441/14/7/1021

[26] R. Gerardo and I. P. de Lima, "Monitoring duckweeds (Lemna minor) in small rivers using sentinel-2 satellite imagery: Application of vegetation and water indices to the lis river (Portugal)," *Water*, vol. 14, no. 15, p. 2284, Jul. 2022, doi: 10.3390/w14152284.

[27] S. Bid and G. Siddique, "Identification of seasonal variation of water turbidity using NDTI method in panchet Hill dam, India," *Model. Earth Syst. Environ.*, vol. 5, no. 4, pp. 1179–1200, Dec. 2019.

[28] M. Bartoli, M. Faggioli, E. Severini, C. Ferrari, J. Bianchetti, M. Lanzoni, M. Magri, M. Pinardi, B. Grandi, and R. Bolpagni, "Analisi ecologiche e misure di portata per la definizione dei fattori correttivi nel calcolo dei deflussi nel mincio e la calibrazione dei sistemi di misura," in *Proc. Valli Del Mincio-Un Delicato Equilibrio*, 2022, pp. 99–99.

[29] E. Soana, E. Racchetti, A. Laini, M. Bartoli, and P. Viaroli, "Soil budget, net export, and potential sinks of nitrogen in the lower oglio river watershed (Northern Italy)," *CLEAN Soil*, vol. 39, no. 11, pp. 956–965, 2011.

[30] R. A. Kristanti and T. Hadibarata, "Phytoremediation of contaminated water using aquatic plants, its mechanism and enhancement," *Current Opinion Environ. Sci. Health*, vol. 32, Apr. 2023, Art. no. 100451. [Online]. Available: https://www.sciencedirect.com/science/article/pii/S2468584423000119

[31] Å. N. Austin, J. P. Hansen, S. Donadi, and J. S. Eklöf, "Relationships between aquatic vegetation and water turbidity: A field survey across seasons and spatial scales," *PLoS ONE*, vol. 12, no. 8, Aug. 2017, Art. no. e0181419.

[32] P. S. Hooda, A. C. Edwards, H. A. Anderson, and A. Miller, "A review of water quality concerns in livestock farming areas," *Sci. Total Environ.*, vol. 250, nos. 1–3, pp. 143–167, Apr. 2000. [Online]. Available: https://www.sciencedirect.com/science/article/pii/S0048969700003739

G. TRIBOLI received the master's degree (cum laude) in information science from the University of Milan. He is currently pursuing the Ph.D. degree in computer and data science. He is a Senior Teacher of computer science and technology with Italian Scientific High Schools. He published some research articles and presented them at several conferences. His current research interests include the Internet of Things, livestock waste management, remote sensing, and environmental pollution monitoring.

M. PICONE received the M.Sc. degree (cum laude) in computer engineering and the Ph.D. degree in information technology from the University of Parma. He is currently an Associate Professor with the Distributed and Pervasive Intelligence (DIPI) Group, Department of Sciences and Methods for Engineering (DISMI), University of Modena and Reggio Emilia. He has also been a Research Visitor with the NetOS Group, Computer Laboratory, University of Cambridge, U.K. He published several research articles and participated in many editorial activities for international journals, conferences, and events. His current research interests include distributed systems, the Internet of Things, edge/fog computing, and digital twins.

M. BERTOGNA received the Ph.D. degree in computer science from the Scuola Superiore Sant'Anna, Pisa, in 2008. He is currently a Full Professor with UNIMORE and the Leader of the HiPeRT Laboratory. He is also the CEO and Founder of HiPeRT Srl (an academic spin-off). He authored more than 100 articles and coordinated multiple EU and industrial projects. His main research interests include high-performance real-time systems, especially based on multi- and many-core devices, autonomous driving, and industrial automation systems.